

Image and Localization of Behind-the-Wall Targets Using Collocated and Distributed Apertures

Yimin D. Zhang and Allan Hunt

Introduction

The technologies described in this chapter are to image, localize, and track behind-the-wall targets, which are either stationary or in motion, using an array with collocated or distributed apertures. Surveillance through obstacles such as walls, doors, and other visually opaque materials using microwave signals is considered as a powerful tool for a variety of applications in both military and commercial paradigms. Through-the-wall imaging has recently been identified as valuable in rescue missions, behind-the-wall target detection, surveillance, and reconnaissance [Hun04, AA06b, AA08].

Radar imaging achieves its range and cross-range resolution of targets through the exploitation of, respectively, the bandwidth of the signals and the aperture of an array of sensors used in the operation. The spatial dimension, or aperture, of the array can be achieved using a collocated physical array or a synthetic array with moving sensors. The range resolution of a radar system is approximately $c/2B$, where c is the speed of propagation and B is the signal bandwidth. The cross-range resolution is approximately $\lambda R/D$, where λ is the wavelength, R is the range, and D is the aperture size of the array.

Depending on the application requirement and the system feasibility, an antenna array can be designed in one- or two-dimensions, or as a set of sparsely distributed sensors. A synthetic array

allows the construction of a large, virtual, aperture from one, or a small number of, physical antennas. A large synthetic aperture size permits high cross-range resolution, even operated from a large stand-off distance [AA08]. Array aperture can be more effectively constructed using bistatic and multi-input multi-output (MIMO) radar processing techniques [LS09].

The data collected at different sensors may be processed coherently or noncoherently. Coherent signal processing utilizes the phase information of the data and achieves better performance. However, it requires high-accuracy phase synchronization and calibrated positioning of the array sensors. Noncoherent signal processing may yield inferior performance, but it does not require phase synchronization among the array sensors. Depending on the dynamics of the targets, wideband signals can be implemented in the time domain, such as using narrow pulses or sweeping chirp (i.e., linear frequency modulated (LFM)) waveforms, or in the frequency domain by using stepped-frequency continuous-wave (CW) signals or a set of subband waveforms [Sko08].

For localization and tracking of a small number of targets in a sparse scene, it becomes possible and more convenient to exploit compression in the data collection and processing. Such techniques include the reduction of the number of time samples, thinned array, and thinned frequency steps, depending on the applications and waveforms being used (see Chapter 14 of this book for more details). An extreme example, which is introduced in this chapter, is the dual-frequency radar that uses two CW signals with separate frequencies to provide range information of a single target or a small number of targets [AAZ07, ZAA08]. Some variants of the dual-frequency radar, including multi-frequency radar and narrowband frequency-hopping radar, are also introduced [LZA09, ZAA08c]. Both schemes improve the unambiguous estimation of target range, and the later also allows frequency agility for low probability of intercept and enhanced jammer resistance.

Targets in motion demonstrate Doppler signatures which, through the appropriate exploitation of the Fourier transform or time-frequency analysis, can be useful for clutter suppression, signal enhancement, and target discrimination [ZAA08]. Fourier transform of the return signal is useful for periodically rotating targets, such as ceiling fans, which generate discrete frequency components, whereas time-frequency analysis techniques find applications in analyzing the time-varying Doppler signatures for moving targets (a detailed discussion is available in Chapter 15 of this book). Targets with different Doppler signatures may be separated in the frequency or time-frequency domain and their localization becomes feasible, even only with a small number of frequencies and array antennas.

1. Radar Imaging

1.1 Coherent Radar Imaging

We first consider the concept of coherent radar imaging that exploits wideband narrow-pulse signals [AA08]. Consider in general a radar imaging system consisting of an M -element transmit array and an N -element receive array, as shown in Fig. 1. The locations of the transmit elements and receive elements are precisely known. The region to be imaged is located along the positive z -axis. Let a transmit element, placed at the m -th transmit location $\mathbf{x}_{t_m} = (x_{t_m}, z_{t_m})$, illuminate the scene with a wideband signal $s_m(t)$. The reflection by any target located in the region being imaged is collected at the N receive elements, located at $\mathbf{x}_{r_n} = (x_{r_n}, z_{r_n})$, $n=1, \dots, N$. For the case of a single point target p located at $\mathbf{x}_p = (x_p, z_p)$, i.e., $i=p$ in Fig.1, the output of the n -th receiver is given by

$$y_{mn}(t) = a(\mathbf{x}_p) s_m(t - \tau_{p,mn}), \quad (1)$$

where $a(\mathbf{x}_p)$ is the complex reflectivity of the point target. The wideband signal, $s_m(t)$, is a narrow pulse that provides the desired range resolution. The propagation delay $\tau_{p,mm}$, encountered by the signal as it travels from the m -th transmit element to the target located at \mathbf{x}_p , and back to the n -th receive element, is given by

$$\tau_{p,mm} = \frac{r_{m,p,air,1} + l_{n,p,air,1}}{c} + \frac{r_{m,p,wall} + l_{n,p,wall}}{v} + \frac{r_{m,p,air,2} + l_{n,p,air,2}}{c}, \quad (2)$$

where c is the speed of propagation in the air, and $v = c/\sqrt{\varepsilon}$ is the speed of propagation in the wall with a dielectric constant ε . The variables $r_{m,p,air,1}$, $r_{m,p,air,2}$, and $r_{m,p,wall}$ represent the traveling distances of the electromagnetic wave in the air and wall, respectively, from the m -th transmit element to the target p , whereas $l_{n,p,air,1}$, $l_{n,p,air,2}$ and $l_{n,p,wall}$ are the traveling distances of the wave in the air and wall, respectively, from the target p to the n -th receive element. The traveling distances inside and outside the wall, and subsequently, the delays in equation (2), can be precisely computed, given the exact knowledge of the wall parameters [AAK03].

[FIGURE 1 HERE]

The M transmit elements can sequentially emit signals to avoid interference between them. That is, only one element is active at a time. For a time slot in which the m -th transmit element is active, the signals received at the N receive elements are coherently processed as follows. The region of interest is divided into a finite number of pixels (for two-dimensional imaging of range and cross-range) or volume pixels, known as voxels (for three-dimensional imaging of range, cross-range, and height). The complex composite signal corresponding to the image of the pixel located at \mathbf{x}_q is obtained by applying time delays and weights to the data at the N receive elements,

performing matched filtering, and summing the results. The system output is given by

$$z_m(\mathbf{x}_q) = \sum_{n=1}^N w_{rn} \int_0^T y_{mn}(t + \tau_{q,mn}) s_m^*(t) dt, \quad (3)$$

where w_{rn} is the weight applied to the output of the n -th receive element, and T is the coherent integration time. The focusing delay $\tau_{q,mn}$ is applied to the output of the n -th receive element when the transmit element is at the m -th location. This delay, which is given by

$$\tau_{q,mn} = \frac{r_{m,q,air,1} + l_{n,q,air,1}}{c} + \frac{r_{m,q,wall} + l_{n,q,wall}}{v} + \frac{r_{m,q,air,2} + l_{n,q,air,2}}{c}, \quad (4)$$

synchronizes the arrivals at different receive locations for the same pixel and, as such, allows coherent imaging of the scene. The variables in equation (4) are the same as those used in equation (2), except the target pixel p is replaced by the focusing pixel q .

When there is only one target, equation (3) becomes

$$z_m(\mathbf{x}_q) = \sum_{n=1}^N w_{rn} a(\mathbf{x}_p) \int_0^T s_m(t - \tau_{p,mn} + \tau_{q,mn}) s_m^*(t) dt = \sum_{n=1}^N w_{rn} a(\mathbf{x}_p) p_m(\tau_{p,mn} - \tau_{q,mn}), \quad (5)$$

where $p_m(t)$ is the output of a matched filter applied to the received signal $s_m(t)$. Therefore, if $\mathbf{x}_p = \mathbf{x}_q$, then the focusing delay $\tau_{q,mn}$ becomes equal to the target propagation delay $\tau_{p,mn}$, and the matched filter output reaches its maximum value at zero-lag. If $\mathbf{x}_p \neq \mathbf{x}_q$, the focusing delay differs from the propagation delay, and the signals in equation (5) are incoherently combined, leading to a much lower matched filter output. In essence, the above coherent combining of target returns is equivalent to forming a beam at pixel \mathbf{x}_p in range and angle directions. The range resolution can be enhanced by using a larger bandwidth pulse, whereas the angular resolution can be improved by increasing the transmit and/or receive array apertures. The latter is discussed in details in Chapter 3 of this book.

By repeating the above process for all the M transmit elements which sequentially switch to

transmit at their respective locations, we can produce M complex composite signals, $z_m(\mathbf{x}_q)$, $m=1,2,\dots,M$, corresponding to the image of the pixel at \mathbf{x}_q . Thus, the final complex signal corresponding to the pixel located at \mathbf{x}_q is obtained by the coherent weighted linear combination

$$z(\mathbf{x}_q) = \sum_{m=1}^M w_{im} z_m(\mathbf{x}_q) = \sum_{m=1}^M \sum_{n=1}^N w_{im} w_{rn} a(\mathbf{x}_p) p_m(\tau_{p,mn} - \tau_{q,mn}), \quad (6)$$

where w_{im} is the weight applied to the component signal $z_m(\mathbf{x}_q)$ obtained using the m -th transmit element. The weights w_{im} and w_{rn} are independent of the pixel location \mathbf{x}_q , and serve to define the system point spread function according to desired specifications. The process described by Equations (3)-(6) is performed for all pixels in the region of interest to generate the composite image of the scene. The general case of multiple targets can be obtained by superposition of target reflections.

1.2 Orthogonal Waveforms for Simultaneous Signal Transmission

In Section 1.1, we assumed that the M transmit elements become active in a sequential order. This method is simple, but is not time efficient because it takes M revisits to complete the signal transmission. A more efficient method is to adopt orthogonal waveforms such that

$$\int_0^T s_m(t) s_l^*(t + \tau) dt = 0 \text{ for any } \tau, \text{ where } m \neq l, m, l = 1, \dots, M. \text{ Waveform orthogonality can be}$$

achieved by utilizing degree-of-freedom in the fast-time as well as the slow-time domains. In practice, perfect orthogonality over all the time delays is infeasible, but it is possible to design waveforms with a sufficiently low cross-correlation to produce an operational system. When all the M transmit elements are active and transmit waveforms $s_m(t)$, $m=1, \dots, M$, the signal received at the n -th receive element is

$$y_n(t) = \sum_{m=1}^M y_{mn}(t) = \sum_{m=1}^M a(\mathbf{x}_p) s_m(t - \tau_{p,mn}). \quad (7)$$

To compute the image value at pixel q , located at \mathbf{x}_q , the above received signal is compensated for using the delay $\tau_{q,mn}$, and then processed with a filter matched to the m -th transmit signal waveform. The weighted sum of the matched filter outputs becomes

$$z_m(\mathbf{x}_q) = \sum_{n=1}^N w_n \int_0^T y_n(t + \tau_{q,mn}) s_m^*(t) dt = \sum_{n=1}^N w_n a(\mathbf{x}_p) p_m(\tau_{p,mn} - \tau_{q,mn}), \quad (8)$$

which is identical to equation (5). Thus, by using M matched filters at the output of each receive element, the responses corresponding to the M transmitted waveforms can be separated for coherent combining, as depicted in equation (6). In this way, we can achieve the same radar imaging capability while the data collection time is reduced by a factor of M , compared to the operation mode that assumes sequential switching at the transmit elements.

1.3 Wall Consideration

For an electromagnetic wave traveling through multiple media with different speeds, the wave propagation path is no longer straight. Consider the wave propagation between a wall with dielectric constant ε and air with dielectric constant $\varepsilon_2 = 1$. The incident angle $\theta_{m,i}$ and the refraction angle $\varphi_{m,i}$, as shown in Fig. 1, are related by Snell's law,

$$\sin \theta_{m,i} = \sqrt{\varepsilon} \sin \varphi_{m,i}. \quad (9)$$

Similar relationship can be established between $\theta_{n,i}$ and $\varphi_{n,i}$. The loss of signal power, change in propagation speed, and the bending effect of the wave as it propagates through and out of a dielectric medium are important factors that must be taken into account for reliable and accurate imaging. Failure to do so would result in errors in the focusing delays for a designated pixel which,

in turn, cause errors in determining the locations of the targets, as shown in [WAZ06, AAM07] and discussed in Chapter 3 of this book. This fact can also be utilized to estimate the wall parameters, when they are unknown, through image sharpness measures if well localized targets can be used as reference [WAZ06, WA06].

To determine the actual path length and the propagation time, angles $\theta_{m,i}$ (or $\phi_{m,i}$) and $\theta_{n,i}$ (or $\phi_{n,i}$) should be identified. Applying the cosine law to the triangle with vertices (\mathbf{A} , \mathbf{B} , \mathbf{x}_i) in Fig. 1, we obtain

$$[x_i - (x_{t_m} - z_{t_m} \tan \theta_{m,i})]^2 + z_i^2 = l_{m,i,wall}^2 + l_{m,i,air,2}^2 - 2l_{m,i,wall}l_{m,i,air,2} \cos(\pi + \phi_{m,i} - \theta_{m,i}), \quad (10)$$

where

$$l_{m,i,wall} = \frac{d}{\cos \phi_{m,i}} \quad \text{and} \quad l_{m,i,air,2} = \frac{z_i - d}{\cos \theta_{m,i}}, \quad (11)$$

with d denoting the wall thickness. Equation (11) is a transcendental equation in the unknown $\theta_{m,i}$ and can be solved numerically by, for example, using the Newton method. Similar solutions can be obtained for $\theta_{n,i}$.

1.4 Noncoherent Radar Imaging

Coherent radar imaging, as discussed above, can provide high range and cross-range resolutions. However, this is achieved at the expense of cost, portability, and increased complexity of the transmitter/receiver design. Noncoherent processing, which is based on the envelope of the signals and does not include phase information, has practical advantages over coherent processing, when considered for through-the-wall radar sensing [AA06]. Noncoherent schemes, though suboptimal, significantly relax the radar positioning and processing requirements, resulting in low cost,

reduced hardware complexity, and portable solutions for through-the-wall imaging and localization. The interest for the use of noncoherent radar imaging system also lies in robustness of the image quality with respect to wall parameter estimation errors and antenna location errors. Precise estimation of the thickness and dielectric constant of an unknown wall is often difficult. Some walls may be inhomogeneous in their material as well as thickness, causing the wall parameter estimation problem to become more challenging. Antenna location error is a particularly significant issue when dealing with synthetic aperture arrays, where positioning of antenna elements in the accuracy of a small fraction of the wavelength is often impractical. Noncoherent imaging technique does not require stringent requirements about the accuracy of the antenna trajectory and altitude, because a small error of the range estimation in the order of a fraction of the wavelength will not be an issue in computing the noncoherent radar images [ACC98].

Similar to equation (6), a noncoherent image is obtained by scanning the area of interest according to the following formula

$$z(\mathbf{x}_q) = \sum_{m=1}^M \sum_{n=1}^N |w_{tm} w_{rn} a(\mathbf{x}_p) p_m(\tau_{p,mn} - \tau_{q,mn})|^\alpha, \quad (12)$$

where the value of α is usually set to 1 or 2.

1.5 Stepped Frequency Approach

In the above discussions, wideband signal waveforms are implemented as narrow pulses. Alternatively, a wideband signal waveform can be synthesized by using other approaches. Noise radar that uses pseudo-random waveforms are introduced in Chapter 5 of this book. Another commonly used approach is to use stepped-frequency signals which approximate a wideband

signal using a finite number K of monochromatic signals with evenly spaced frequencies f_k covering the desired bandwidth $f_{K-1} - f_0$, where $f_k = f_0 + k\Delta f$ for $k = 0, 1, \dots, K-1$, with

$\Delta f = \frac{f_{K-1} - f_0}{K-1}$ representing the frequency step size. For a stepped-frequency waveform, the

range resolution is determined by the bandwidth of the waveform and is given by

$$\Delta R = \frac{c}{2(K-1)\Delta f} = \frac{c}{2(f_{K-1} - f_0)}. \quad (13)$$

There is range ambiguity associated with the stepped-frequency signal. For two narrowband signals separated in frequency by Δf , the maximum unambiguous range is given by

$R_{\max} = c/(2\Delta f)$. Therefore, the frequency step size is set by the maximum desired unambiguous range as,

$$\Delta f \leq \frac{c}{2R_{\max}}. \quad (14)$$

The above condition allows the backscattered signals from the farthest range of interest R_{\max} to reach the receiver before the signal source switches to the next frequency. As an example, for a stepped-frequency signal of 1 GHz bandwidth, the step-size required to image all ranges up to 30 m is 5 MHz, which amounts to using 201 frequency steps.

Stepped-frequency operation has several advantages. Most importantly, a wideband waveform is synthesized by a sequence of instantaneous narrowband signals. As such, it achieves the same effect as that of short-duration pulses while avoiding the difficulties associated with the use of short-time duration signal. Further, the stepped-frequency implementation of wideband waveforms allows changing the emitted power over the signal bandwidth. We can, therefore, compensate for the frequency-dependent power attenuation of the wall, limiting the signal time-dispersion and preserving the shape and duration of the intended pulse as it travels through

the wall. On the other hand, a key limitation of stepped-frequency operation lies in the dynamic range requirement. This is further discussed in the next section.

2. Performance Limitations in Practical Imaging Systems

There is a wide variety of potential applications for through-the-wall imaging systems that come with different performance requirements. System range, resolution, size, speed of operation, and cost among others can all be traded off during the system design process. It is important to understand the performance limitations that are imposed by these different requirements in order to be able to select the system configuration appropriate for the application of interest. This section addresses hardware, algorithm, and system configuration issues that are important to the system design process. Some key issues addressed are the use of time-domain (narrow pulse) waveforms versus frequency-domain (stepped-frequency) waveforms, system design options and implications, specialized hardware techniques for improving system dynamic range, performance of algorithms for imaging and localizing moving and stationary targets, and exploitation of distributed apertures for imaging. Examples from existing hardware systems are used to illustrate these issues.

2.1 Effects of System Design on Imaging System Performance

Both frequency-domain and time-domain methods can be used for through-the-wall imaging sensors. System performance is determined by the choice of hardware elements and their arrangement in the imaging system.

In time-domain impulse systems, the transmitter is relatively easy to implement from a hardware point of view while the receiver is much more complex. Since the receiver frontend must be broadband in order to cover the bandwidth of the transmitted impulses, these systems are susceptible to strong interfering signals anywhere in the band of the transmitted impulses. Hardware methods to filter specific frequencies to minimize interference are impractical.

Many impulse system implementations do not provide phase information associated with the received signal. This makes it difficult to apply corrections to the received signal to account for frequency-dependent system effects associated with antenna and electronics performance, and reduces the effectiveness of integration to improve image formation results.

For frequency-domain systems, the hardware implementation for both the transmitter and receiver is moderately difficult. Like impulse systems, the frontend must be broadband. However, detection is performed over a very narrow band thus limiting interference effects to specific frequencies. Phase information is preserved in the detected signal for most frequency-domain systems. This makes it easier to apply corrections to the received signal to account for frequency-dependent system effects, and enhances the ability to improve image processing through coherent integration.

Table 1 shows a set of possible sensor configurations that can be used to illustrate the effect system design has on operational performance and on the elements of the hardware system that affect performance. Using a single radar, with a switch to scan an antenna array, is attractive since the amount of hardware is minimized. However, it takes longer to collect the full frame of data required for detection processing. In a frequency-domain implementation, system sensitivity is set by the spacing between adjacent antennas. Improving the isolation between antennas by increasing spacing allows the dynamic range to be increased.

The single-transmitter multiple-receiver approach has the advantage that it allows data to be collected from all antennas in parallel, reducing the time to collect the full frame of data required for detection processing. However, in order to preserve coherent detection, it is necessary to provide all of the receivers with common clock and local oscillator signals. Without a common local oscillator, the spurious noise components in each receiver are not coherent and will not be removed during change detection processing. Receiving in parallel allows more data to be collected during any processing interval than that for the scanned array system, and improves the SNR. This comes at the cost of more hardware and more computation for real-time operation.

The independent radar approach, with a radar for each antenna, allows for radars to move independently and work cooperatively to perform imaging and detection. However, this configuration requires that the internal clocks of the radars be synchronized in order to maintain coherent operation, and that the antenna positions can be accurately located with respect to one another in order to perform image processing. As in the multiple receiver configuration, each radar sensor receives at the same time, improving the SNR. Even though the hardware is more complex and costly and the processing more difficult in this configuration, it allows a wider range of operational options because of the cooperative nature of its architecture.

[PLACE TABLE 1 HERE]

Antenna selection and array configuration will introduce system specific performance effects. System cross-range resolution is set by the antenna array aperture and the lowest frequency of operation. Aliasing in cross-range is determined by the spacing between the antennas in an array and will show up as artifacts during image reconstruction that can be misinterpreted as targets.

For frequency-domain approaches antenna array spacing presents an additional problem. Antenna spacing determines system sensitivity since the direct path between transmit and receive antennas is the largest signal received and sets the upper limit of the receiver dynamic range. In addition to limiting dynamic range, this signal, when transformed to the time domain, has a sharp rise time and creates a $\sin(x)/x$ response often referred to as range sidelobes. For static imaging, this response is a “noise” source, and will obscure small targets that are close in range. When performing change detection for detecting movement, however, this noise disappears because it is coherent. Time-domain systems do not have this problem since the receiver is turned off while the transmitter is on.

Improving system performance by reducing the magnitude of the direct path signal can be achieved passively, by increasing the separation between antennas, or actively, through special hardware design. One active technique, using pulse modulation, was originally developed by Burnside [Whi85, Cla92, Mas95, San05] for use in compact radar ranges with stepped-frequency radar systems. A block diagram of this technique is shown in Figure 2. The hardware consists of a network of switches that are inserted between the antennas of the system and its signal generation and detection electronics. This allows the system to operate in a manner similar to time-domain systems by inhibiting reception while the transmitter is on and inhibiting transmission while the receiver is on. The transmit/receive switching cycle is performed at a rate much higher than the frequency stepping time, resulting in a pulse modulated frequency output. Pulse modulation creates high-frequency sidebands, however, these fall outside of the receiver intermediate frequency bandwidth and do not show up in the detected signal. There is a duty cycle loss associated with the fraction of time the transmitter is off during a pulse modulation interval.

Pulse modulation provides the opportunity to improve system performance substantially.

Without a large direct path signal, it is possible to add low noise amplification (LNA) in the receive side which both improves system noise figure and adds system gain. Power amplification (PA) in the transmit side can be used to make for the pulse modulation duty cycle loss and increase system transmit power over the maximum possible without using pulse modulation. As with a time-domain impulse system, however, a primary limitation of the pulse modulation technique is how close in range imaging can be performed. This is determined by the speed of the switches used.

[PLACE FIGURE 2 HERE]

Figure 3 shows experimental data from a stepped-frequency CW system where pulse modulation has been implemented. A radar was set up in front of a concrete wall and operated with 1) no pulse modulation, 2) pulse modulation but no compensation for duty cycle loss through PA and/or receive side LNA, and 3) pulse modulation with duty cycle loss compensation and receive side LNA. For both pulse modulation cases the direct path signal has been reduced by 43 dB. With PA to compensate for duty cycle loss and LNA, the SNR of the wall is approximately 20 dB greater than without pulse modulation.

[PLACE FIGURE 3 HERE]

An alternate technique for reducing the antenna direct path signal is through active antenna nulling. In this method, the transmitted signal is sampled and added back into the receive channel with the same amplitude but 180° out of phase. Figure 4 shows data from a system that

implements this technique. In this case the direct path reduction is 25 dB. A sphere 4 meters in front of the system shows an improvement in SNR of 10 dB for the nulling case. The advantage of this type of direct path signal mitigation is being able to image at much closer ranges than the pulse modulation technique, although this technique has traditionally been very difficult to implement for wideband systems.

[PLACE FIGURE 4 HERE]

Finally, careful design of the antenna is also important for both frequency- and time-domain systems. If the impedance of the antenna selected is not well matched to the impedance of the transmitting power amplifier, false targets will be generated in the received waveform due to secondary reflections of the transmitted waveform caused by the impedance mismatch.

2.2 Imaging Approaches to Target Localization

Data collected with stationary array systems or with moving arrays can be used to form images to locate stationary and moving targets. The image resolution in range and cross-range that can be achieved is determined by the system operating parameters. Image reconstruction can be accomplished using either frequency-domain or time-domain techniques. The back-projection method [Nat86] is commonly used for stepped-frequency systems because of its simplicity and computational efficiency. For systems with multiple antennas where all of the antennas are used to both transmit and receive, a complete image frame consists of the addition (coherent or noncoherent) of the subimages (one transmitter and all receivers) from all of the $(N_t) \times (N_r - 1)$ combinations of transmitters and receivers. If a system has been implemented using the pulse

modulation technique described above, then it is possible to both transmit and receive on the same antenna during a single frequency sweep. Under this condition a complete image frame will consist of the addition of the subimages from $(N_t \times N_r)$ combinations of transmitters and receivers. As the number of antennas increases, it is possible to get good results using the subimages. The subimage can be immediately displayed while the data for the next subimage is being taken. As additional subimages are added to the image, the SNR improves and the stationary features in the imaged scene become more evident. Sensitivity to target motion is not high because the most current image is not weighted heavily. If there are moving targets, they will leave a trail in the image.

Motion detection is performed using complete image frames. In its simplest implementation, this is accomplished by subtraction of adjacent images in a sequence. If $X(n)$ is the full-spectrum image sequence, then the first-order motion detection image can be expressed as:

$$Z(n) = X(n) - X(n-1).$$

Higher-order detectors are more stable with better SNR, but they are less sensitive. The second-order motion detection image can be expressed as:

$$Z(n) = 0.5X(n) - X(n-1) + 0.5X(n-2).$$

It is possible to superimpose motion profiles on the underlying static image $Y(n)$, where $Y(n)$ has been formed by averaging several previous full image frames $X(n)$. The common approach is to form the display image expressed as:

$$D(n) = a|Z(n)| + (1-a) |Y(n)|,$$

where a is the parameter, bounded between 0 and 1, that controls the threshold for visualization.

Larger a emphasizes the changes due to motion with relatively light background profiles. When $a = 1$, only motion is displayed. In order to reduce confusion, it is often the case that color is used to

represent the motion term $Z(n)$, and grey scale is used to represent the static image term $Y(n)$.

Figure 5 shows an example of the display of superimposed motion and static images for large motions. The display in the left side of the figure is an image, formed using the first-order motion detection technique, of the instantaneous position of a person walking around a room. Data was collected over the frequency range of 500 MHz to 1 GHz. In this image, the static image of a concrete wall at 15 meters is not well focused because of poor low-frequency phase center characteristics of the system antennas. The right side of the figure is a display of the history of movement created by finding the location of the person in each image of the sequence and using a simple weighted average of the previous 10 positions.

[PLACE FIGURE 5 HERE]

Small motions can also be detected by first- and second-order change detection algorithms. Figure 6 shows how the signal magnitude of a change detected target varies as a function of the amount of movement between successive image frames. The first-order algorithm is more sensitive to very small motions than the second-order algorithm. Since the magnitude of the change-detected signal depends on the SNR of the data collected by the radar system, the amount of motion that is detectable will be determined by target size, distance, wall thickness, and sensitivity of the imaging radar.

[PLACE FIGURE 6 HERE]

Figure 7 shows an example of small motion detection from a test using a machine to simulate

the breathing of a person. The breathing machine consists of a 0.43 meter diameter slightly convex metal plate attached to a linear bearing that is driven by an electric motor and eccentric cam. It was placed 0.2 meter behind a 0.15 meter thick concrete block wall filled with concrete and steel reinforcing bar. The total amplitude of motion was 2.54 cm at a frequency of 0.26 Hz. A radar with a four antenna array was placed 50 meters from the wall. On the left side of the figure is a display of the real time range profile from a single antenna combination. To the right of the figure is the superimposed static and change detection image formed in real time. The wall and the moving plate clearly imaged.

[PLACE FIGURE 7 HERE]

Conventional synthetic aperture radar (SAR) processing can also be used for localizing targets through walls and can be performed with a single pair of antennas or an array. Using an array helps fill the aperture and improves SNR. Moving the radar has the advantage that the resolution in cross-range can be improved because the effective aperture of the antenna array can be increased. To perform successful imaging, however, it is necessary to know the position of the antennas during each data collection period so that the data can be registered accurately. An inexpensive method of keeping track of vehicle position (for a ground system) is by using information from encoders attached to the wheels of the vehicle. Encoders can provide more accurate position information in real time than a GPS/INS system but provide only the relative position of the vehicle with respect to the structure being imaged. Residual motion of the antennas due to movement over uneven surfaces will cause defocusing of the reconstructed image. One method of measuring the instantaneous position of the antenna array to determine pitch, roll, and

yaw is by using commercially available three axis motion measurement integrated circuits.

Figure 8 shows an image generated from a vehicle mounted, horizontal, 2.2 m long, 6-antenna array system of a fire training tower with 0.2 m thick concrete walls containing both vertical and horizontal steel reinforcement. Operating frequency of the radar was 500 MHz to 2 GHz and the vehicle was equipped with a set of shaft encoders that gave a vehicle position uncertainty of 2.8 cm. The synthetic aperture of the generated the image was 20 m. No corrections have been made to the image to account for frequency-dependent dispersion effects.

[PLACE FIGURE 8 HERE]

2.3 Distributed Aperture Systems

Distributed aperture systems have the advantage of being able to improve the resolution of an imaging system. The moving platform image shown in Figure 9 is an example of antenna distribution in the cross-range dimension. Antennas can be distributed in the range and height dimensions as well. As indicated earlier, however, using widely spaced systems puts an additional burden on the hardware and the requirement to accurately locate antenna positions so that image reconstruction is successful. Figure 9 shows a comparison of two simulation results where 8 antennas were distributed linearly along one axis, and randomly around three sides of a set of point scatterers. The scatterers are much better focused for the random placement of antennas even though there are the same number as in the linear array.

[PLACE FIGURE 9 HERE]

To illustrate the potential benefits of the distributed array approach, experimental data was collected with two 4-element systems on the concrete fire tower structure imaged in Figure 8. The systems were set up at a standoff of 15 m on two sides of the fire tower as shown in the photograph of Figure 10. Data were collected simultaneously from both systems of a stationary individual standing inside the fire tower, and combined coherently. Both walls and the individual are clearly seen with the location resolution of the individual much improved over the single array case shown earlier in Figure 5. Even though this experiment involved a simple distributed system, it shows the benefits that can be achieved as hardware capabilities continue to evolve.

[PLACE FIGURE 10 HERE]

3 Target Range Estimation and Localization

When a single target or a small number of targets are of interest, a simpler alternative is to localize the individual targets rather than image the entire area. Target localization can be based on the combination of direction-of-arrival (DOA) and range information measured at one or multiple positions, or range-only or DOA-only information measured at multiple positions through, respectively, trilateration and triangulation. Methods that use combined DOA and range information and that use range-only information are introduced in Section 3.1 and Section 3.2 respectively.

3.1 Target Localization Based on DOA and Range Information

When both the DOA and range information of a target is available at a radar, the location of the

target can be uniquely determined. Depending on the applications, the DOA can be one-dimensional (typically azimuth-only), or two-dimensional (azimuth and elevation). When omni-directional antenna elements are used, the minimum number of elements required for one-dimensional DOA estimation is two, whereas for two-dimensional DOA estimation, at least three non-collinearly located elements are required. The principle is illustrated in Fig. 11 for a one-dimensional DOA scenario in a plane coordinate system, where $p_1 = (x_1, y_1)$ is the position of the radar, and $p = (x, y)$ is the unknown position of the target.

[PLACE FIGURE 11 HERE]

Denote the DOA of the backscattering signal from the target as α with respect to the horizontal axis of the reference coordinate and the estimated range as d . The target coordinates are obtained as

$$x = x_1 + d \cos \alpha, \quad y = y_1 + d \sin \alpha. \quad (15)$$

When the range and direction information is available at M reference points $p_i(x_i, y_i)$, $i = 1, \dots, M$, the target location can be estimated by solving the following equations

$$x = x_i + d_i \cos \alpha_i, \quad y = y_i + d_i \sin \alpha_i, \quad i = 1, \dots, M, \quad (16)$$

where d_i and α_i are, respectively, the range and DOA of the target measured at the reference point p_i . The least-square solution of equation (16) is given by

$$x = \frac{1}{M} \sum_{i=1}^M (x_i + d_i \cos \alpha_i), \quad y = \frac{1}{M} \sum_{i=1}^M (y_i + d_i \sin \alpha_i). \quad (17)$$

In [LL06] and [RLL08], radar systems using an array consisting of three non-collinearly located antenna elements are reported. The DOA information is obtained from the array based on phase difference information between the signal received at the different elements, whereas the range information is based on the phase information using two CW signals transmitted and received at one element. The dual-frequency range estimation technique exploiting two CW signals is introduced in Section 3.3, and the utilization of Doppler signature for the enhancement and discrimination of target signal is introduced in Section 4.

3.2 Target Localization through Trilateration

Localization of stationary and moving targets using noncoherent techniques has been extensively studied in the context of through-the-wall surveillance [AA06, AA06b, AAS06, ZAA08, ZAA08b]. The trilateration/multilateration method determines the position of a target using the range information estimated at several spatially separated radar points.

Consider a target in a two-dimensional space as illustrated in Figure 12. Denote (x,y) as the location of the target, and its distance to the i -th radar, located at (x_i,y_i) , as d_i . In the presence of $M \geq 3$ radars, the target location can be determined by solving the following three equations

$$(x - x_i)^2 + (y - y_i)^2 = d_i^2, \quad i = 1, \dots, M. \quad (18)$$

[PLACE FIGURE 12 HERE]

When $M = 3$, the solution is given by [STK05]

$$\begin{pmatrix} x \\ y \end{pmatrix} = \mathbf{A}^{-1} \mathbf{b}, \quad (19)$$

where

$$\mathbf{A} = \begin{pmatrix} x_1 - x_2 & y_1 - y_2 \\ \vdots & \vdots \\ x_{M-1} - x_M & y_{M-1} - y_M \end{pmatrix}, \quad (20)$$

and

$$\mathbf{b} = \frac{1}{2} \begin{pmatrix} d_2^2 - d_1^2 + x_1^2 - x_2^2 + y_1^2 - y_2^2 \\ \vdots \\ d_M^2 - d_{M-1}^2 + x_{M-1}^2 - x_M^2 + y_{M-1}^2 - y_M^2 \end{pmatrix}, \quad (21)$$

provided that matrix \mathbf{A} is full rank. When $M > 3$ radars are available, it becomes an over-determined problem, and the least-square solution of equation (18) is obtained as

$$\begin{pmatrix} x \\ y \end{pmatrix} = (\mathbf{A}^T \mathbf{A})^{-1} \mathbf{A}^T \mathbf{b}, \quad (22)$$

where $(\cdot)^T$ denotes the transpose of a matrix or a vector.

3.3 Range Estimations

3.3.1 Range Estimation Based on TOA Estimation

When a wideband signals are used, the range information of a target can be estimated from the times-of-arrival (TOA). In this case, the magnitude of the output signal at a receiver, after matched filtering, can be used for peak detection. For example, consider a monostatic radar in the absence

of a wall, the range estimate is related to the round-trip propagation delay τ by $d = c\tau/2$. When a wall is involved, the effect of wall can be properly considered as described in Section 1.

3.3.2 Range Estimation Based on Dual-Frequency Processing

For the range estimation of a single target, an alternative is to use a small number of CW waveforms. We start with the introduction of the dual-frequency radar system, followed by other variants. A dual-frequency radar simultaneously measures the phase change, with respect to time, for each of the two frequencies. The range is estimated based on the phase difference between the two frequencies [Boy63, AAZ07]. Due to phase wrapping in the observed return signals, there exists the range ambiguity problem. The maximum unambiguous range of the target is determined by the separation between the two distinct carrier frequencies.

Consider a dual-frequency CW radar operating at frequencies f_1 and f_2 . The baseband radar return at frequency f_i can be expressed as,

$$s_i(t) = \rho_i(t) \exp(-j\phi_i(t)), \quad i = 1, 2, \quad (23)$$

where $\rho_i(t)$ and $\phi_i(t) = 4\pi f_i R(t)/c$ are, respectively, the range-dependent amplitude and the phase of the return signal corresponding to the i -th frequency of operation, and $R(t)$ is the range of the moving target.

Without considering phase wrapping, range $R(t)$ can be estimated from the phase difference observed at the return signal corresponding to the two frequencies, i.e.,

$$R(t) = \frac{c[\phi_2(t) - \phi_1(t)]}{4\pi(f_2 - f_1)}. \quad (24)$$

With phase wrapping, the true phase is expressed as

$$\phi^{(true)}(t) = \phi_2(t) - \phi_1(t) + 2m\pi, \quad (25)$$

where m is an unknown integer. Accordingly, the range estimate is subject to range ambiguity [AAS06, RLL08], i.e.,

$$R(t) = \frac{c[\phi_2(t) - \phi_1(t)]}{4\pi(f_2 - f_1)} + \frac{cm}{2(f_2 - f_1)}. \quad (26)$$

The second term in the above equation induces ambiguity in range. For the same phase difference, the range can assume infinite values separated by

$$R_{\max} = \frac{c}{2(f_2 - f_1)}, \quad (27)$$

which is referred to as the maximum unambiguous range.

Depending on the application, sufficient unambiguous range may be achieved by properly selecting the frequency difference between the two carriers. For example, a 10MHz difference in the carrier frequencies yields a 15m unambiguous range. Depending on the dimension of the structure under investigation, this unambiguous range may be sufficient to uniquely solve for the target range, given prior knowledge of the structure bounds on target location. The bounds determine the integer value m corresponding to the possible target range.

The choice of the specific values of f_1 and f_2 can be made based on RF wall penetration and design issues of the radar units. A small frequency separation will yield a large unambiguous range estimation. A small frequency separation, however, will reduce the sensitivity of the phase difference with respect to the range and thus compromise the range estimation performance[LZA09].

3.3.3 Range Estimation Based on Multi-Frequency Processing

There are a number of reasons to use composite CW waveforms with more than two frequencies.

One apparent advantage of using multiple frequency components is to achieve frequency diversity against noise and propagation fading. Through-the-wall radar systems are often operated in a low SNR environment due to wall attenuation and other factors, and thus the phase information may not be reliable. Multipath propagation may further introduce frequency-dependent fading, causing very weak signals in some frequencies. By using M equally spaced frequencies,

$f_0, f_0 + \Delta f, \dots, f_0 + (M - 1)\Delta f$, where Δf is the difference between two adjacent carrier

frequencies, the phase differences obtained from the $M-1$ pairs with adjacent frequencies can be fused to yield robust range estimation against noise and frequency-selective multipath fading. One way to fuse these data is through a weighted average of the range estimates, with a high weight being assigned to the strong frequency pairs and a low weight to the weak ones [LZA09]. When there is a possibility of having significant errors, outlier analysis that excludes abnormal data is helpful. When equally spaced frequencies are used, the maximum unambiguous range remains $c/(2\Delta f)$, which is the same as a dual-frequency radar with frequency separation of Δf .

Another important feature of using multi-frequency signaling is to increase the unambiguous range by exploiting nonuniformly spaced frequencies [WXC04, XW07]. It is clear from equation (26) that the sensitivity of range estimation error is inversely proportional to the frequency separation [LZA09]. Therefore, while it may be necessary to use a pair of frequencies with a small separation for larger unambiguous range, a large frequency separation is often desirable to reduce the range estimation error. When this tradeoff is difficult to achieve, a solution is to use more than two CW signals, yielding multi-frequency radar for range estimation [WXC04, XW07, LZA09].

For the k -th frequency pair consisting of adjacent frequencies, i.e., f_k and f_{k+1} , $k = 1, \dots, M-1$, a wrapped phase difference is observed as $\Delta\phi_k = \phi_{k+1} - \phi_k$. Then, the range of the target is related to the phase observation by

$$R(t) = \frac{c\Delta\phi_k(t)}{4\pi\Delta f_k} + \frac{cm_k}{2\Delta f} = \frac{v_k\Delta\phi_k(t)}{4\pi} + \frac{v_k m_k}{2}, \quad (28)$$

where $\Delta f_k = f_{k+1} - f_k$ and $v_k = c/\Delta f_k$. If we choose v_k as a multiple of a constant Δ_d , which represents a range bin width, we can express v_k as $v_k = \xi_k \Delta_d$, where ξ_k is a nonnegative integer. As such, the maximum unambiguous range obtained from the k -th pair of frequencies is expressed as

$$R_{\max,k} = \frac{c}{2\Delta f_k} = \frac{v_k}{2} = \frac{\xi_k \Delta_d}{2}. \quad (29)$$

Therefore, the maximum unambiguous range of the multi-frequency radar becomes

$$R_{\max} = \frac{\Delta_d}{2} \text{LCD}(\xi_1, \xi_2, \dots, \xi_{M-1}), \quad (30)$$

where $\text{LCD}(\cdot)$ denotes the lowest common denominator operator, and the minimum distance between two adjacent ambiguous target range estimates is given by

$$D_{\min} = \frac{\Delta_d}{2} \text{GCD}(\xi_1, \xi_2, \dots, \xi_{M-1}), \quad (31)$$

where $\text{GCD}(\cdot)$ denotes the greatest common divisor operator. Specifically, by choosing co-prime

values of ξ_k for $k=1, 2, \dots, M-1$, we obtain $R_{\max} = \frac{\Delta_d}{2} \prod_{k=1}^{M-1} \xi_k$ and $D_{\min} = \frac{\Delta_d}{2}$. As a result, the

unambiguous range can be significantly increased. In this scheme, Δ_d should be properly chosen such that range estimation does not erroneously fall into other range bins.

3.3.4 Range Estimation Based on Frequency-Hopping Signals

While dual- and multi-frequency radars are relatively simple, they suffer from some shortcomings as well. First, because of wrapping in phase measurement, the range ambiguity problem may demand the use of a smaller frequency separation in a dual-frequency radar, but doing so will

undesirably degrade the range estimation accuracy in the presence of measurement noise [LZA09]. This problem is greatly eased with the use of multiple frequencies, but a multi-frequency radar may not completely solve the range ambiguity problem if the random range estimation error exceeds the range bin resolution. Second, the waveforms of dual- and multi-frequency radars are not constant modulus, and the peak-to-average power ratio (PAPR) increases as more frequencies are used. This imposes a high linearity requirement on the system. The requirement for simultaneous filtering and isolating different components of the received signals is another burden for hardware implementations. Third, the high spectral density of the radar signal waveform at the operating carriers may create significant interference to environment and increase radar detectability by intelligent adversaries.

Narrowband frequency-hopping (NB-FH) radars were developed by switching the CW frequency over time within the available frequency band [ZAA08c]. NB-FH radars achieve several advantages compared to dual- and multi-frequency radar systems: (1) Utilizing a range of hopping frequencies, it overcomes the range ambiguity problem. (2) The signal waveform is instantaneously narrowband and contains only one frequency component at a time. As such, an NB-FH radar can be implemented with a lower complexity compared to wideband radars as well as dual- and multi-frequency radars. (3) Compared to dual- and multi-frequency radars, the NB-FH radar approach spreads the signal energy over the bandwidth and thus significantly reduces the peak power spectrum density. As such, owing to spreading of the spectrum similar to the process adopted in spread spectrum communication signals, the sensing operation generates less interference to the environment, becomes more covert due to reduced probability of intercept and probability of detection, and increases the immunity to interference and jamming.

4 Time-Frequency Analysis for Moving Target Localization

In through-the-wall applications, direct use of the received signal observed from a dual- or multi-frequency radar is often impractical because of the low SNR and thus the phase information is highly perturbed. In addition, the received signal may include significant contributions from clutter, or other targets in the scene. When moving targets are of interest, appropriate use of time-frequency analysis of the Doppler signatures can facilitate significant SNR enhancement, clutter suppression, and target separation and discrimination.

4.1 Time-Frequency Representations

Moving targets generate Doppler shift in the backscattered signals. Depending on the maneuvering nature of the target, the Doppler frequency may be constant or time-varying. The former occurs when, for example, the target motion is in the same direction, relative to the observation radar, with a constant velocity. In this case, the Fourier transform of the observation results in coherent integration, and therefore a gain in SNR, at a specific Doppler frequency. The Fourier transform well characterizes the Doppler signature of the target. When multiple targets with different constant Doppler frequencies are present, the Fourier transform also provides the capability for target separation and discrimination.

When the Doppler frequency is time-varying, which occurs, e.g., when the target moves with a nonconstant speed, the Fourier transform is no longer the most suitable analysis tool. For example, when the Doppler frequency of a target varies from 100 Hz to 200 Hz over a period of time, the spectrum obtained from Fourier transform will bears no distinction to the result of another target whose Doppler frequency varies from 200 Hz to 100 Hz over the same time span. Therefore, the

Fourier transform fails to represent the maneuvering behavior of the target which is key for SNR enhancement as well as target characterization and discrimination.

For such non-stationary signals with time-varying Doppler frequency, it is desirable to use signal representations in the joint time-frequency domain. Time-frequency representations map one-dimensional signals in the time domain into two-dimensional signal representations in the time-frequency domain. The property of concentrating the input signal energy around its instantaneous frequency while spreading the noise energy over the entire time-frequency domain increases the effective SNR and proves valuable in range and DOA estimations [ZAA08, ZMA01].

The most commonly used time-frequency representations include linear transforms, such as short-time Fourier transform (STFT), Gabor transform, and wavelet transform, and bilinear (or quadratic) transforms, such as Wigner-Ville distribution and Cohen's class of generalized time-frequency distributions [Coh89, Coh95]. The STFT of a signal $x(t)$ can be defined as

$$F_x(t, f) = \int_{-\infty}^{\infty} x(\tau)h(\tau - t)e^{-j2\pi f\tau} d\tau, \quad (32)$$

where $h(t)$ is the window function. The use of different windows allows trading-off the time and frequency resolutions. Satisfactory time and frequency resolutions require proper selection of the sampling rate and the window function. Generally, when the Doppler frequency changes slowly, a large window size would yield high frequency resolution. When the Doppler frequency varies rapidly, a small window size would ensure the spectrum does not smear over different frequency bins.

The Cohen's class of bilinear time-frequency distribution of two narrowband signals $x_i(t)$ and $x_k(t)$ is defined as [Coh89, Coh95]

$$D_{x_i x_k}(t, f) = \iint \phi(t-u, \tau) x_i(u + \frac{\tau}{2}) x_k^*(u - \frac{\tau}{2}) e^{-j2\pi f \tau} du d\tau, \quad (33)$$

where $\phi(t, \tau)$ is the time-frequency kernel, τ is the time-lag variable, and $(.)^*$ denotes complex conjugation. When $x_i(t)=x_k(t)=x(t)$, the result is the auto-term time-frequency distribution of $x(t)$, whereas when the two signals differ, it becomes their cross-term time-frequency distribution.

When comparing linear and bilinear time-frequency representations, STFT is relatively simple to compute, but its major disadvantage lies in the necessity to trade-off the time and frequency resolutions for rapidly time-varying Doppler signatures. Bilinear time-frequency representations provide better localization of signal energy for chirp-like Doppler signatures, but they generally require high computations. The existence of cross-terms between multi-component signals is often undesirable and a number of time-frequency kernels are developed to reduce such effect [KCB92, Coh95].

To illustrate the advantages of using time-frequency representations in range estimation, we consider a range estimation problem based on dual-frequency processing, as introduced in Section 3.3.2. For a signal waveform expressed in equation (23), the Doppler frequency shift can be obtained as

$$f_{D,i}(t) = -\frac{1}{2\pi} \frac{d\phi_i(t)}{dt} = -\frac{2f_i}{c} \frac{dR(t)}{dt}. \quad (34)$$

There are a few different ways to benefit from the time-frequency analysis of the Doppler signature for range estimations. In the following, we first consider the range estimation based on the phase information of STFT (Section 4.2) and cross-term distribution of bilinear time-frequency representations (Section 4.3). The range estimation utilizing the Doppler frequency signatures is discussed in Section 4.4.

4.2 Range Estimation Based on STFT Phase Information

For an LFM signal, the phase information is preserved at the STFT result when it is obtained using a symmetric window about the time instant of interest. As a result, instead of using in equation (26) the phase delay difference between the backscattered signals corresponding to the two carrier frequencies for each time instant, the difference in the phase of their respective STFT results can be effectively used to estimate the range.

For a backscattered signal with a moderate SNR, the detection of the STFT peaks that reflect the true signal power concentration is straightforward. For weak signals, however, the detection of such STFT peaks may not be always reliable. One of the techniques that can be used to further enhance the SNR for improved peak detection is to average the magnitude of the STFT results obtained from all the available frequencies. The advantage of such averaging becomes more pronounced in a multi-frequency radar. Due to the frequency resolution limitation, the STFT signature of $s_2(t)$ may approximately coincide with that of $s_1(t)$. In this case, direct averaging can be performed. In some situations, however, the STFT corresponding to the true signal signatures may not overlap. In this case, the STFT signatures corresponding to all the frequencies can be aligned through scaling and interpolating the time axis of the received signal at each frequency.

4.3 Range Estimation Based on Phase Information of Bilinear Time-Frequency Distribution

The respective bilinear time-frequency distributions of received signals $s_1(t)$ and $s_2(t)$, described in equation (23), will show strong presence around their respective instantaneous frequencies. The auto-terms, however, are real valued and do not provide the phase information required for range estimation. Rather, the cross-term time-frequency distribution between backscattered signals $s_1(t)$

and $s_2(t)$ results in a concentrated presence in the time-frequency domain, located in the middle of the two auto-term distributions, with the phase information representing the phase difference between the two carriers. Therefore, similar to STFT, this information is more robust to noise and can be used for range estimation as well.

4.4 Range Estimation Based on Doppler Signatures

An alternative way to utilize the Doppler signature for range estimation is to estimate the phase information from the Doppler frequency. For a dual-frequency radar, we obtain from equation (34) that

$$\phi_i(t) = \phi_i(0) - 2\pi \int_0^t f_{D,i}(t) dt, \quad i=1, 2. \quad (35)$$

From equation (34), it is known that the Doppler frequency shift is proportional to the carrier frequency, resulting in the following relationship:

$$f_{D,2}(t) - f_{D,1}(t) = (f_2 / f_1 - 1) f_{D,1}(t). \quad (36)$$

Thus, the phase difference $\phi(t) = \phi_2(t) - \phi_1(t)$ can be expressed as

$$\phi(t) = \phi(0) - 2\pi \int_0^t [f_{D,2}(t) - f_{D,1}(t)] dt = \phi(0) - 2\pi \left[\frac{f_2}{f_1} - 1 \right] \int_0^t f_{D,1}(t) dt. \quad (37)$$

As such, the phase information of the return signals and, subsequently, the ranges of moving targets, can be obtained from the Doppler frequency shift up to an initial value $\phi(0)$. The unknown initial phase difference $\phi(0)$ can be estimated by minimizing the overall distance between $\phi(t)$, obtained from equation (37), and the phase difference directly obtained from the phase of the STFT, $\tilde{\phi}(t) = \tilde{\phi}_2(t) - \tilde{\phi}_1(t)$, at the selected Doppler signatures. That is,

$$\phi(0) = \arg \min_{\phi(0)} \int \|\phi(t) - \tilde{\phi}(t)\|^2 dt, \quad (38)$$

where the integral is evaluated over the entire observation period. Note that a Doppler signature bias may accumulate over time to yield a large error in the range estimate. Therefore, high frequency resolution is desirable in performing the STFT computations.

The phase difference estimation in equation (37) can be based on the Doppler observation at either frequency. Fused results incorporating the Doppler signatures in all the frequencies will yield improved range estimation, particularly in an impaired channel environment [ZAA08d].

4.5 Examples

In this section, we provide a few examples that demonstrate the offerings of time-frequency analysis in a dual-frequency radar [ZAA08]. In the first simulation example, we consider a single target scenario where the target swings around a center which is 5 m away from the radar with a maximum displacement of 1 m. The observation period is 1 second. The two carrier frequencies are 990 MHz and 1 GHz, respectively. It is assumed that, regardless of the range, the reflection coefficient of the target is constant, yielding an input SNR of 0 dB.

Figure 13(a) shows the spectrogram of the received signal at frequency 990 MHz, denoted as $s_1(t)$. The STFT signature of the backscattered signal at frequency 1 GHz, $s_2(t)$, is similar to that of $s_1(t)$. The sampling frequency is 1 kHz, and a 101-point Hanning window is used to perform the STFT. As shown in Fig. 13(a), despite the low SNR level, the Doppler frequency signatures can be clearly identified in the spectrogram. Figs. 13(b)-(d) show the range estimates using raw data, STFT phase, and the Doppler signature. It is evident from Fig. 13(b) that, because of the noise, the raw data based approach fails to provide meaningful range estimates. Significant improvement is

achieved when using the phase information from the STFT. The best results are, however, obtained when the Doppler signature based approach is applied.

[PLACE FIGURE 13 HERE]

Signals backscattered from multiple targets with distinct Doppler signatures may be separated in the time-frequency domain. With the ability of capturing each Doppler signature of the moving targets in the scene, one can proceed to calculate the respective phase information and subsequently estimate the target range.

To illustrate such capacity, we consider a two-target scenario, where the Doppler frequencies of the two targets overlap. A target moves away from the radar at a constant speed of 0.5 m/s, whereas the other target moves away at a time-varying speed, accelerating from 0 m/s to 2 m/s over a period of 5 s. The initial ranges of the two targets are 4.5 m and 4 m, respectively. To clearly illustrate the effect of multiple targets, no noise is considered in this example. Fig. 14(a) shows the spectrogram at the carrier frequency of 990 MHz. Raw data based estimation only yields a single range trajectory in the middle of the true target trajectories (Fig. 14(b)). In the time-frequency domain, the Doppler frequencies of the two targets are separated for most of the observation period, but they overlap at around $t = 1.25$ s. As a result, poor range estimates occur around this moment when the STFT phase information is used, as seen in Fig. 14(c). This problem is overcome by using the instantaneous Doppler signature, as demonstrated by the range estimate in Fig. 14(d).

[PLACE FIGURE 14 HERE]

In the laboratory experiments reported in [ZAA08], a dual-frequency radar with operational frequencies of 919.866 MHz and 906.317 MHz was employed. The surrounding walls of the lab were lined with electromagnetic absorbers to reduce ambient reflections. In the experiment, a conducting sphere of diameter 0.20 m is mounted on a linear positioner, which is controlled to move back and forth over a 3.05 m range with a speed of 0.635 m/s. Thus, it takes approximately 4.8 s for the sphere to travel in each direction. The sampling frequency is 1 kHz and the time duration of the collected data is 20 s. The received baseband data is preprocessed to remove clutter component near the DC frequency before time-frequency analysis and range estimation are performed. Fig. 15(a) shows the spectrogram of the baseband signal corresponding to carrier frequency of 919.866 MHz, where a 2001-point Hanning window is used to perform an 8192-point STFT. The estimated range using raw data is shown in Fig. 15(b), whereas that estimated from the STFT phase difference is shown in Fig. 15(c). Note that, in this experiment, the SNR is relatively high. As a result, range estimation based on raw data is robust, although some local variance is observed. Such variance is not observed in Figs. 15(c) and 15(d) for the result based on time-frequency representations. Interestingly, range estimation results depicted in Figs. 15(b) and 15(c) are affected by a phase distortion due to reflection from a computer rack located in the corner of the lab. The effect of the reflection is observed in Fig. 15(a) as a weak chirp. Such effect is mitigated when the Doppler signature based approach is exploited, as shown in Fig. 15(d).

[PLACE FIGURE 15 HERE]

5. Localization of Inanimate Moving Target Using Dual-Frequency Synthetic Aperture Radar

For inanimate moving targets with periodic rotation pattern, the application of the Fourier transform to the return signal provides enhanced SNR, and allows range estimation of multiple

targets provided that their rotation frequencies differ [RLL08]. In this section, we consider dual-frequency radar exploiting synthetic array aperture as a desirable system configuration [ZAA08b].

Consider a simplified point target model, where the point target rotates according to the following expression:

$$x(t) = x_0 + D \cos(2\pi f_0 t + \phi) \cos(\theta), \quad y(t) = y_0 + D \cos(2\pi f_0 t + \phi) \sin(\theta), \quad (39)$$

where (x_0, y_0) is the coordinate of the rotation center, D is the maximum displacement, f_0 is the rotation frequency, ϕ is the initial phase, and θ represents the direction of rotation.

Let (x_m, y_m) be the coordinate of the m -th radar position. The received signal at the m -th radar position for carrier frequency f_i can be expressed as

$$s_{m,i}(t) = \frac{k}{r_m(t)} \exp\left[j\left(2\pi f_i t - \frac{4\pi r_m(t)}{\lambda_i}\right)\right], \quad i=1, 2, m=1, \dots, M, \quad (40)$$

where k is a constant, λ_i is the wavelength, and $r_m(t) = [(x_m - x(t))^2 + (y_m - y(t))^2]^{1/2}$ is the distance between the target and the m -th radar position.

In this case, the frequency signature is sinusoidally modulated and discrete spectra appear in the integer multiples of the rotation frequency f_0 . Therefore, performing discrete Fourier transform over a long time period yields high peaks at these harmonics for convenient estimation of f_0 . Further, the phase difference at frequency f_0 eliminates the effect of position displacement due to rotation and yields a robust estimate of $r_{m,0} = [(x_m - x_0)^2 + (y_m - y_0)^2]^{1/2}$, i.e., the distance between the target center and the m -th radar position. Once the ranges are estimated, the least-square solutions provided in equation (19) or (22) can be used to estimate the target position from the observations made at the M radar positions.

6. Conclusion

We have examined, from theoretical and practical perspectives, the radar imaging and target localization problems in through-the-wall applications. Range and cross-range resolution requires high bandwidth and large array aperture. Wideband signal can be implemented in the time domain or in the frequency domain, and their respective advantages and disadvantages in practical applications are addressed. A large array aperture is usually achieved using a number of antenna sensors, but synthetic array aperture may also be useful, particularly for the imaging and localization of stationary and inanimate moving targets. When a sparse number of targets are of interest, target localization could lead to a simpler problem. Spectrum and time-frequency analyses are shown to be useful for clutter suppression, SNR enhancement, target discrimination, and target characterization.

References

- [AA06] F. Ahmad and M. Amin, "A noncoherent approach to radar localization through unknown walls," in *Proc. IEEE Radar Conf.*, pp. 583-589, 2006.
- [AA06b] F. Ahmad and M. Amin, "Noncoherent approach to through-the-wall radar imaging," *IEEE Trans. Aerospace Electron. Syst.*, vol. 42, no. 4, pp. 1405-1419, Oct. 2006.
- [AA08] M. G. Amin and F. Ahmad, "Wideband synthetic aperture beamforming for through-the-wall imaging," *IEEE Signal Processing Magazine*, July 2008.
- [AAK03] F. Ahmad and M. G. Amin, S. A. Kassam, and G. J. Frazer, "A wideband, synthetic aperture beamformer for through-the-wall imaging," in *Proc. IEEE Int. Symp. Phase Array Systems and Technology*, Boston, MA, Oct. 2003.
- [AAM07] F. Ahmad, M. G. Amin, G. Mandapati, "Autofocusing of through-the-wall radar

- imagery under unknown wall characteristics,” *IEEE Trans. Image Proc.*, vol. 16, no. 7, pp. 1785-1795, July 2007.
- [AAS06] F. Ahmad, M. Amin, P. Setlur, “Through-the-wall target localization using dual-frequency CW radars,” in *Proc. SPIE*, vol. 6201, Orlando, FL, April 2006.
- [AAZ07] F. Ahmad, M. G. Amin, and P. D. Zeman, “Performance analysis of dual-frequency CW radars for motion detection and ranging in urban sensing applications,” in *Proc. SPIE*, vol. 6547, Orlando, FL, April 2007.
- [ACC98] P. Alais, P. Cervenka, P. Cjallande, V. Lesec, “Noncoherent synthetic aperture Imaging,” in *Proc. Int. Symp. Acoustical Imaging (Acoustical Imaging Volume 24)*, Santa Barbara, CA, Sept. 1998.
- [Boy63] W. D. Boyer, “A duplex, Doppler, phase comparison radar,” *IEEE Trans. Aerospace and Navigational Electronics*, vol. ANE-10, no. 3, pp. 27-33, 1963.
- [Cla92] J. R. Clark, *A High Power Solid State Pulsed-CW RCS Measurement Radar System*, Master’s Thesis, Ohio State Univ., 1992.
- [Coh89] L. Cohen, “Time-frequency distributions – a review,” *Proc. IEEE*, vol. 77, no. 7, pp. 941–981, July 1989.
- [Coh95] L. Cohen, *Time-Frequency Analysis*, Englewood Cliffs, NJ: Prentice Hall, 1995.
- [Hun04] A. R. Hunt, “A wideband imaging radar for through-the-wall surveillance,” in *Proc. SPIE*, vol. 5403, pp.590-596, Apr. 2004.
- [KCB92] P. J. Kootsookos, B. C. Lovell, and B. Boashash, “A unified approach to the STFT, TFDs, and instantaneous frequency,” *IEEE Trans. Signal Processing*, vol.40, no.8, pp.1971-1982, Aug 1992.
- [LL06] A. Lin and H. Ling, “Three-dimensional tracking of humans using a very low-complexity radar,” *Electron. Lett.*, vol. 42, pp. 1062–1064, 2006.
- [LS09] J. Li and P. Stoica (Ed.), *MIMO Radar Signal Processing*. Wiley, 2009.
- [LZA09] X. Li, Y. Zhang, and M. G. Amin, “Multifrequency-based range estimation of RFID tags,” in *Proc. IEEE Int. Conf. RFID*, Orlando, FL, April 2009.
- [Man96] D. E. Manolakis, “Efficient solution and performance analysis of 3-D position estimation by trilateration”, *IEEE Trans. Aerospace Electron. Syst.*, vol. 32, no. 4, pp. 1239-1248, Oct. 1996.

- [Mas95] A. W. Mast, *Development of the Upgraded OSU Pulsed Radar System and Diagnostic Software*, Master's Thesis, Ohio State Univ., 1995.
- [MBV09] D. Munoz, F. Bouchereau, C. Vargas, and R. Enriquez-Caldera, *Position Location Technioiques and Applications*. Academic Press, 2009.
- [Nat86] F. Natterer, *The Mathematics of Computerized Tomography*. New York: Wiley, 1986.
- [Rez00] R. I. Reza, *Data Fusion for Improved TOA/TDOA Position Determination in Wireless Systems*, M.S. Thesis, Virginia Polytechnic Inst. and State Univ., July 2000.
- [RLL08] S. S. Ram, Y. Li, A. Lin, and H. Ling, "Doppler-based detection and tracking of humans in indoor environments," *J. Franklin Inst.*, vol. 345, no. 6, pp. 679-699, Sept. 2008.
- [San05] J. S. Sandora, *Design of the ElectroScience Lab's 0.4 – 100 GHz Compact Range Radar System*, Master's Thesis, Ohio State Univ., 2005.
- [SGG08] Z. Sahinoglu, S. Gezici, and I. Guvenc, *Ultra-wideband Positioning Systems: Theoretical Limits, Ranging Algorithms, and Protocols*. Cambridge, 2008.
- [Sko08] M. Skolnik (Ed.), *Radar Handbook*, 3rd Edition. McGraw Hill, 2008.
- [STK05] A. H. Sayed, A. Tarughat, and N. Khajehnouri, "Network-based wireless location," *IEEE Signal Processing Magazine*, vol. 22, no. 4, pp. 24-40, July 2005.
- [WA06] G. Wang and M. G. Amin, "Imaging through unknown walls using different standoff distances," *IEEE Trans. Signal Processing*, Oct. 2006.
- [WAZ06] G. Wang, M. G. Amin, and Y. Zhang, "A new approach for target locations in the presence of wall ambiguity," *IEEE Trans. Aerospace Electron. Syst.*, vol. 42, no. 1, pp. 301-315, Jan. 2006.
- [Whi85] R. T. Whitacre, *The OSU Pulse/CW Radar for Compact Range Radar Cross Section Measurements*, Master's Thesis, Ohio State Univ., 1985.
- [WXC04] G. Wang, X.-G. Xia, V. C. Chen, and R. L. Fiedler, "Detection, location, and imaging of fast moving targets using multifrequency antenna array SAR," *IEEE Trans. Aerospace Electron. Syst.*, vol. 40, no. 1, pp. 345-355, Jan. 2004.
- [XW07] X.-G. Xia and G. Wang, "Phase unwrapping and a robust Chinese remainder theorem," *IEEE Signal Processing Letters*, vol. 14, no. 4, pp. 247–250, April 2007.
- [ZAA08] Y. Zhang, M. G. Amin, and F. Ahmad, "Time-frequency analysis for the localization of multiple moving targets using dual-frequency radars," *IEEE Signal Processing Letters*,

vol. 15, pp. 777-780, 2008.

- [ZAA08b] Y. Zhang, M. G. Amin, and F. Ahmad, "Localization of inanimate moving targets using dual-frequency synthetic aperture radar and time-frequency analysis," in *Proc. IEEE Int. Geoscience & Remote Sensing Symp.*, Boston, MA, July 2008.
- [ZAA08c] Y. Zhang, M. G. Amin, and F. Ahmad, "Narrowband frequency-hopping radars for the range estimation of moving and vibrating targets," in *Proc. SPIE Symposium on Defense and Security Symposium*, vol. 6947, Orlando, FL, March 2008.
- [ZAA08d] Y. Zhang, M. G. Amin, and F. Ahmad, "Application of time-frequency analysis and Kalman filter to range estimation of targets in enclosed structures," in *Proc. IEEE Radar Conf.*, Rome, Italy, May 2008.
- [ZMA01] Y. Zhang, W. Mu, and M. G. Amin, "Subspace analysis of spatial time-frequency distribution matrices," *IEEE Trans. Signal Processing*, vol. 49, no. 4, pp. 747-759, April 2001.

Tables and Figures
(in low resolution)

System Configuration	Advantages	Disadvantages
Single radar Scanned antenna array	Simple hardware Static or dynamic operation Large aperture synthesized through movement	Sensitivity set by array spacing Shortest detection range
Single transmitter Multiple receivers Scanned antenna array	Static or dynamic operation Large aperture synthesized through movement Longer detection range	More complex hardware Sensitivity set by array spacing Higher computational burden
Independent radars Distributed antenna array	Static or dynamic operation Largest instantaneous aperture Least cross range aliasing	Most complex hardware Most difficult processing

Table 1. Imaging system configurations.

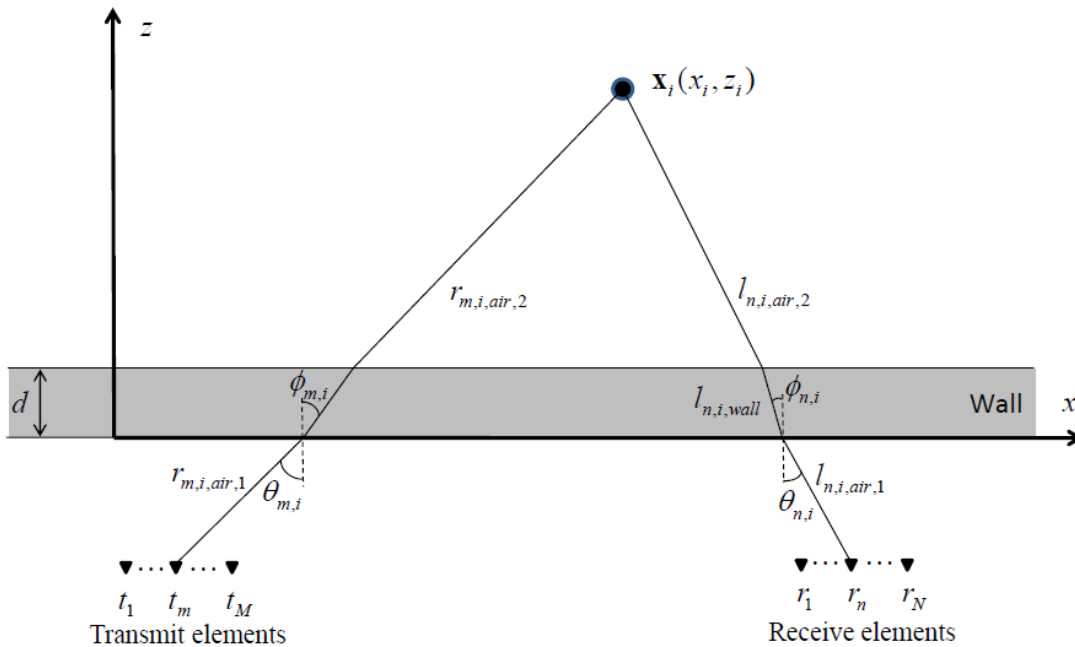


Figure 1. Geometry depicting propagation through a dielectric wall.

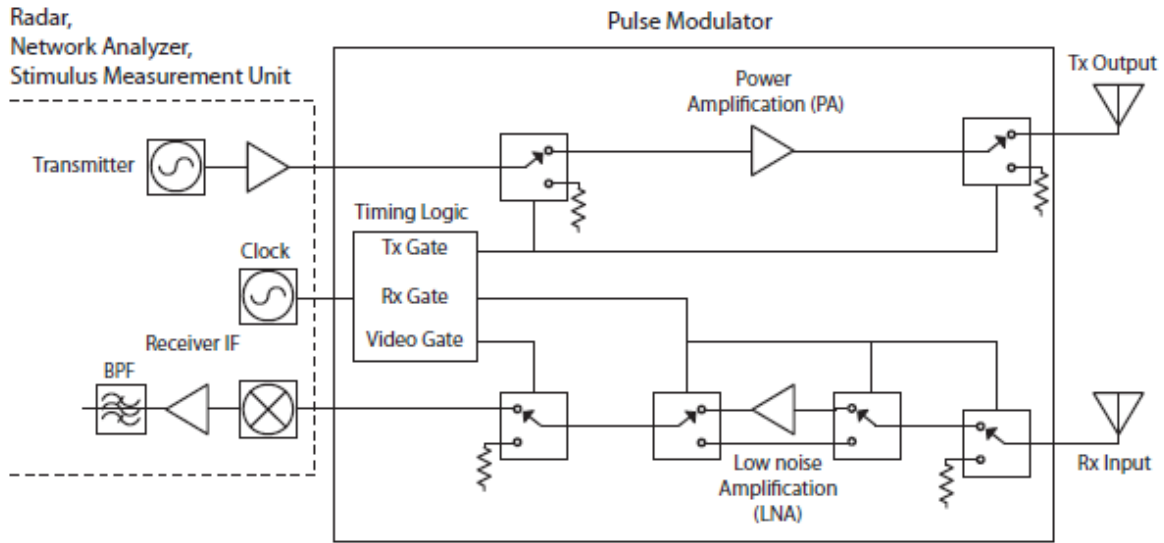


Figure 2. Method for reducing antenna direct path through pulse modulation.

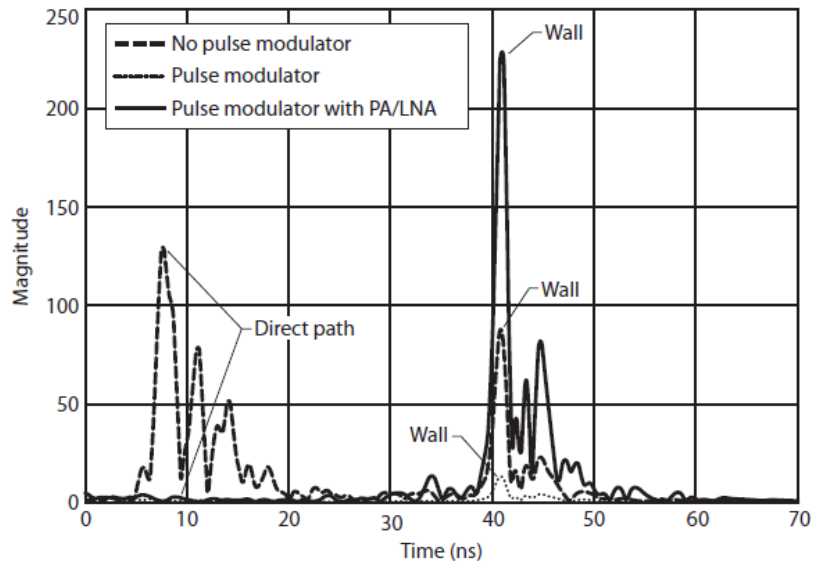


Figure 3. Direct path reduction through pulse modulation.

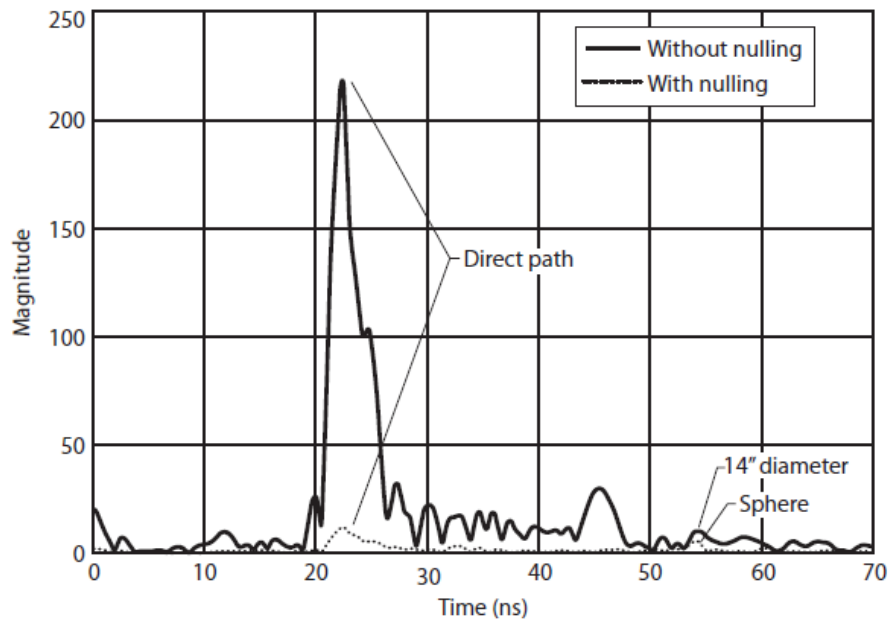


Figure 4. Direct path reduction through active antenna nulling .

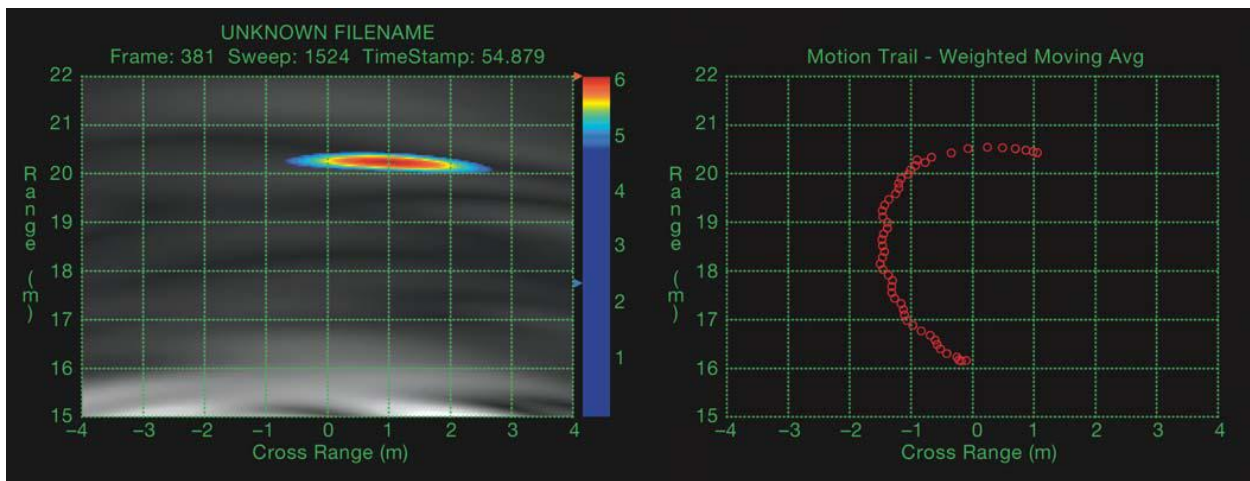


Figure 5. Detection and tracking of large movements.

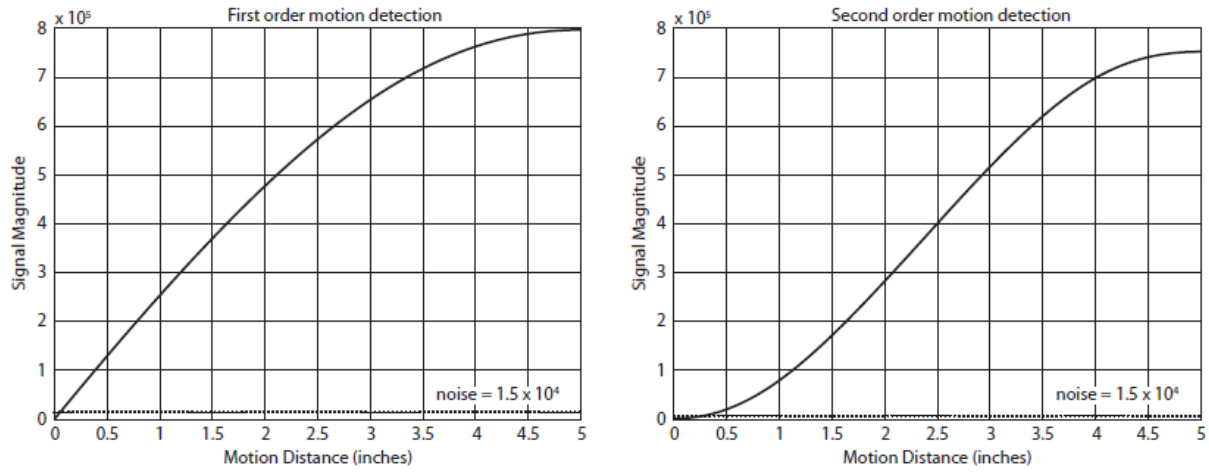


Figure 6. Comparison of motion detection algorithm sensitivity.

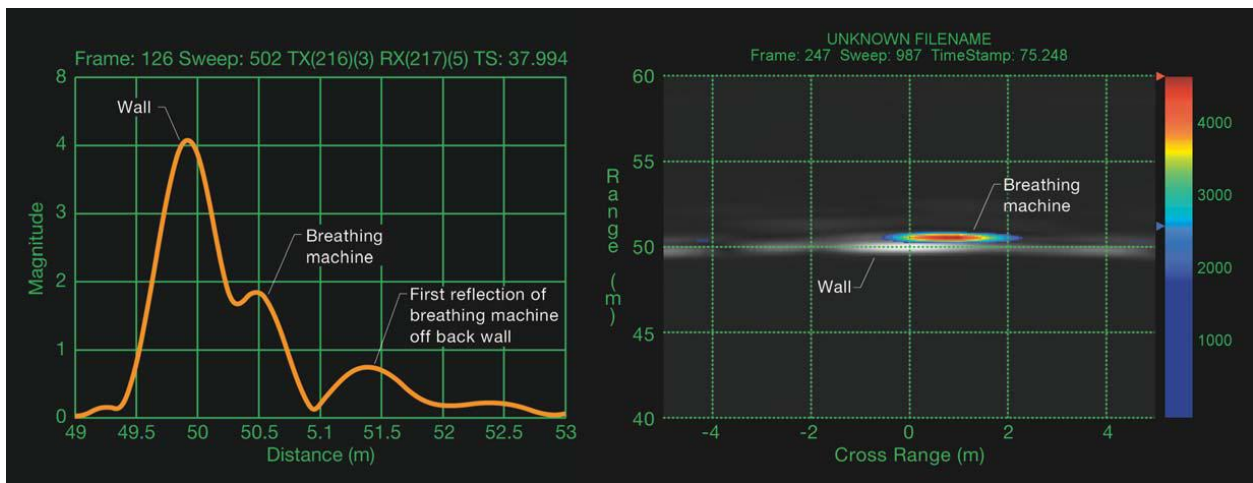


Figure 7. Image formation results showing detection of small motion behind a concrete wall.

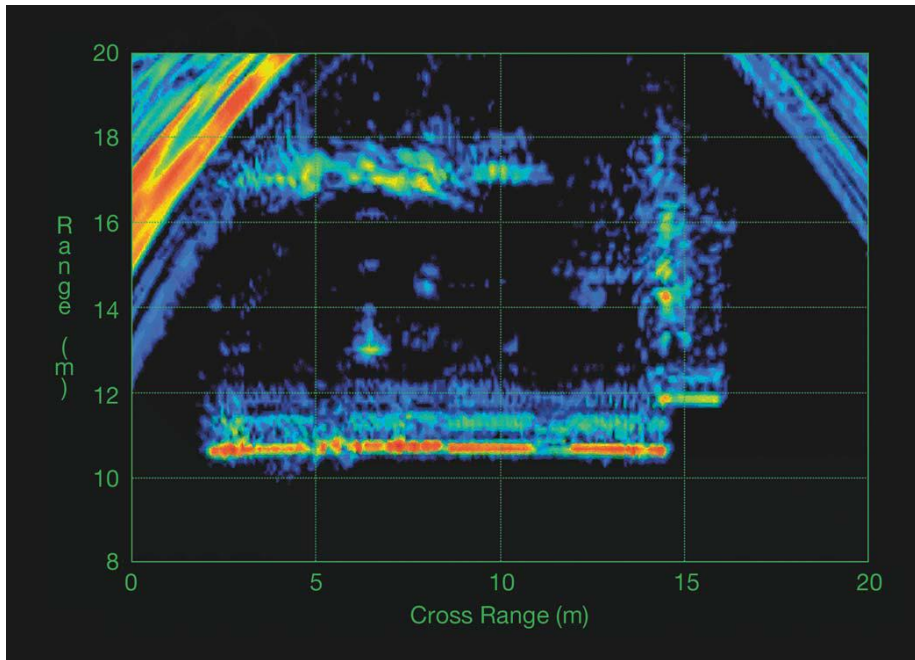


Figure 8. Image of reinforced concrete building.

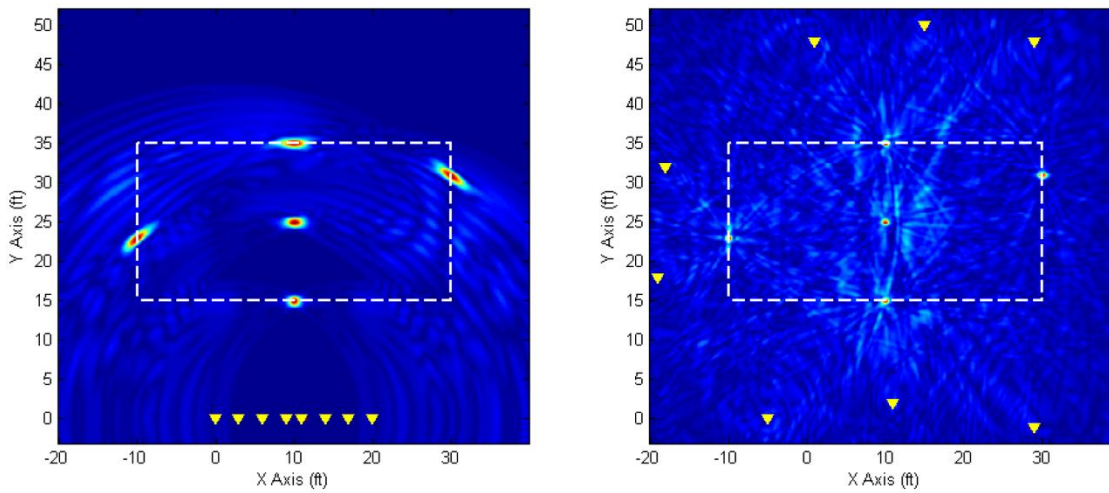


Figure 9 Comparison of linear and random distributed array images .

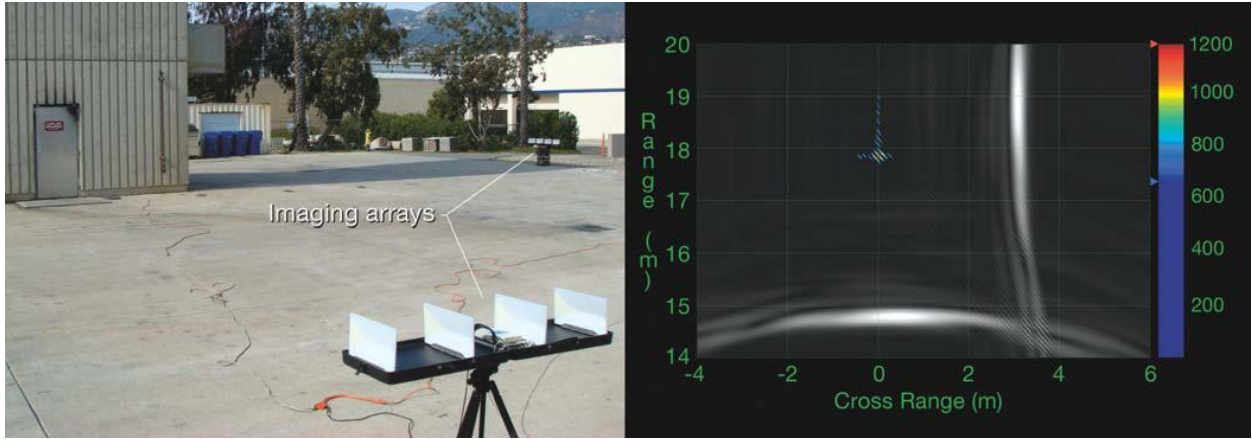


Figure 10. Distributed system imaging results.

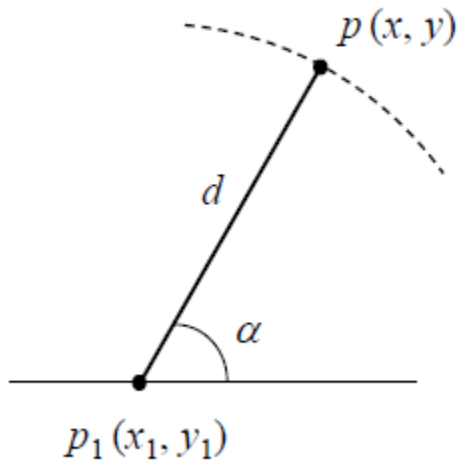


Figure 11. Target localization based on direction and range information.

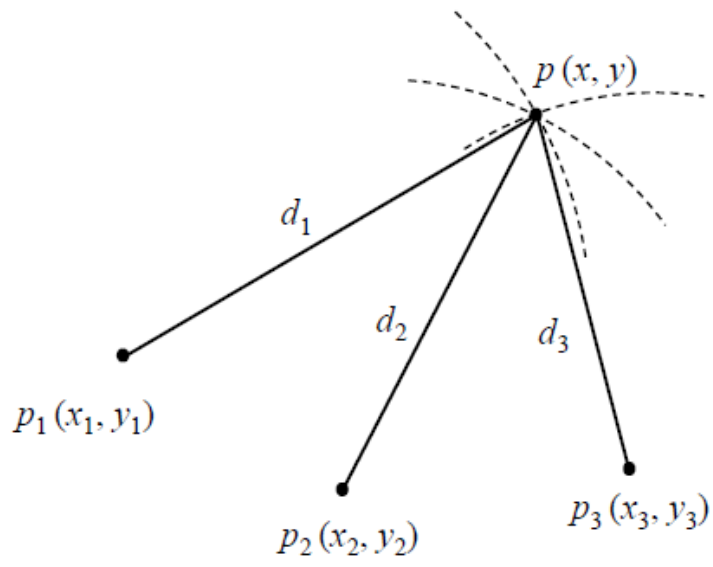
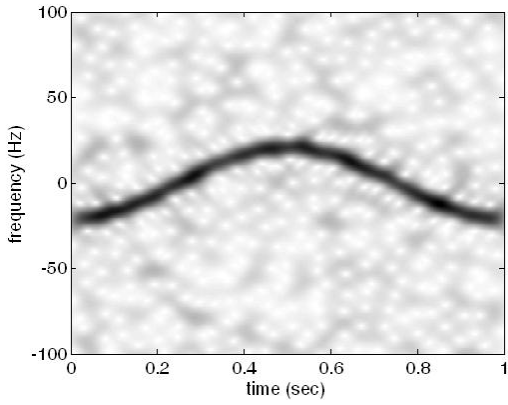
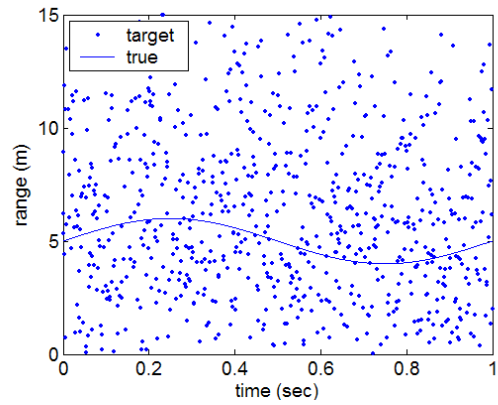


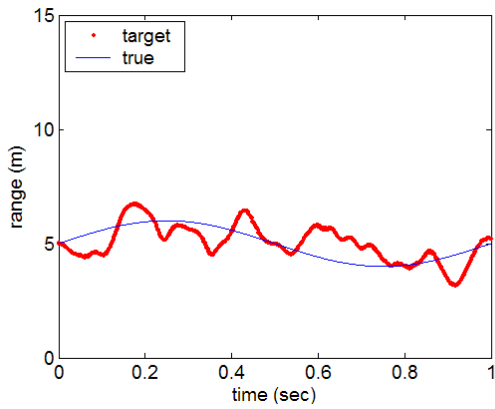
Figure 12. Trilateration using three independent monostatic radar units.



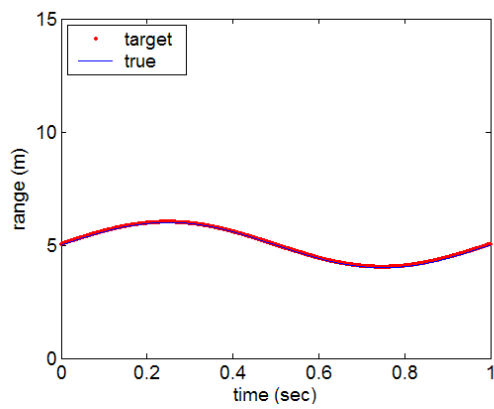
(a) Spectrogram of $s_1(t)$



(b) Range estimate based on raw data

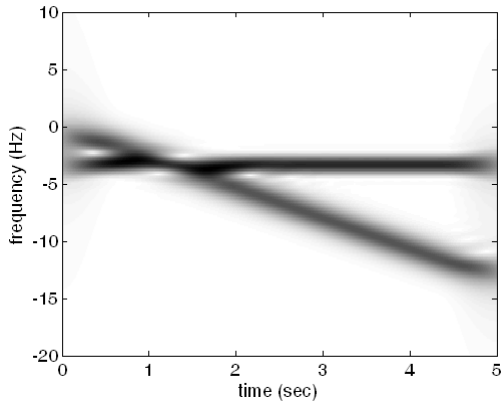


(c) Range estimate based on STFT phase

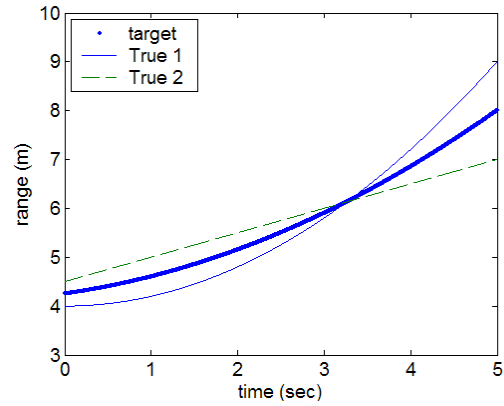


(d) Range estimate based on Doppler signature

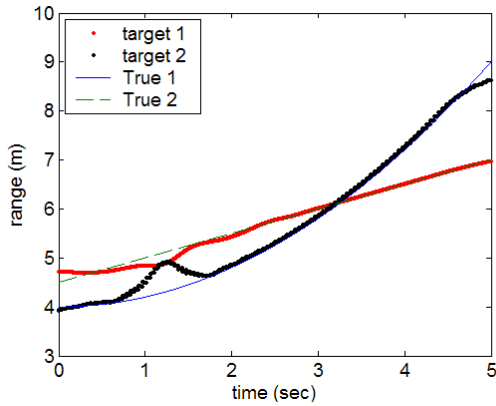
Figure 13. STFT and range estimation results of a single target case in the presence of noise (SNR=0 dB) (Copyright 2008 IEEE [7]).



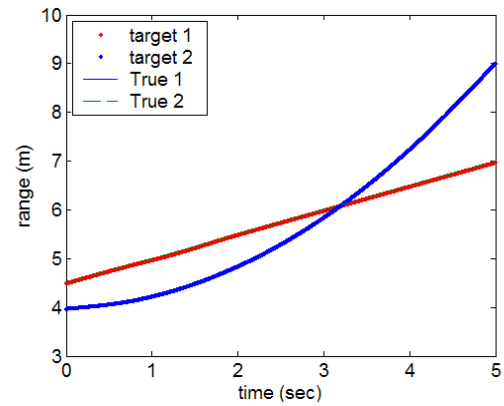
(a) Spectrogram of $s_1(t)$



(b) Range estimate based on raw data

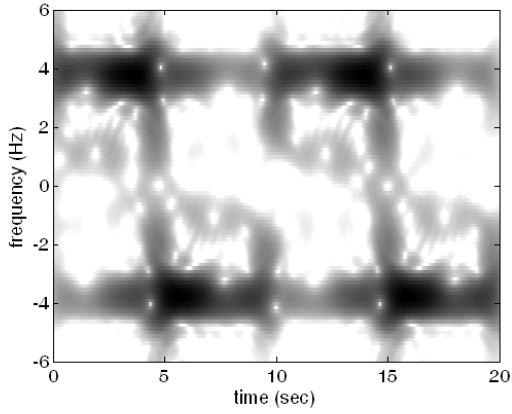


(c) Range estimate based on STFT phase

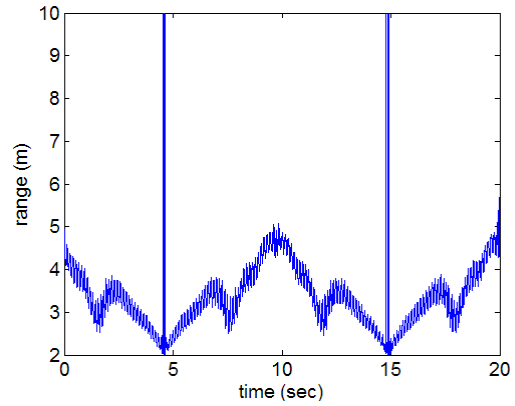


(d) Range estimate based on Doppler signature

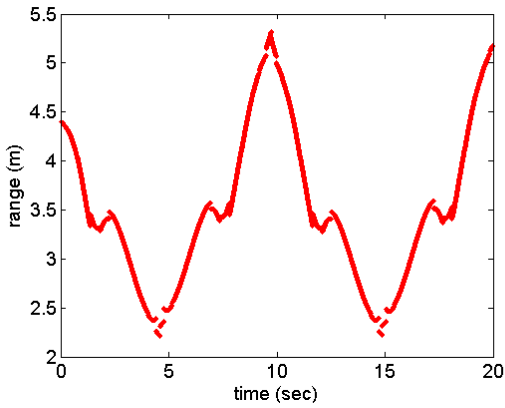
Figure 14. STFT and range estimates of two-targets in the absence of noise. The targets have overlapping Doppler signatures in the time-frequency domain (Copyright 2008 IEEE [7]).



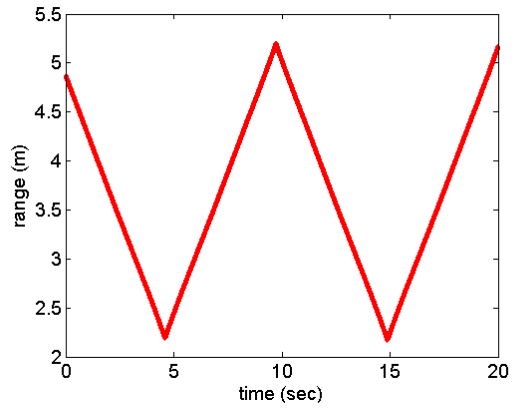
(a) Spectrogram of $s_1(t)$



(b) Range estimate based on raw data



(c) Range estimate based on STFT phase



(d) Range estimate based on Doppler signature

Figure 15. STFT and range estimation results where one conducting sphere moves back and forth (Copyright 2008 IEEE [7]).